Design of photonic crystals with multiple and combined band gaps

Design of photonic crystals with multiple and combined band gaps

H. Men,[1] N. C. Nguyen,[2] R. M. Freund,[3] K. M. Lim,[1] P. A. Parrilo,[4] and J. Peraire[2]
[1]*National University of Singapore, Center for Singapore-MIT Alliance, Singapore 117576*
[2]*MIT Department of Aeronautics and Astronautics, 77 Massachusetts Avenue, Cambridge, Massachusetts 02139, USA*
[3]*MIT Sloan School of Management, 50 Memorial Drive, Cambridge, Massachusetts 02142, USA*
[4]*MIT Department of Electrical Engineering and Computer Science, 77 Massachusetts Avenue, Cambridge, Massachusetts 02139, USA*
(Received 18 September 2010; published 6 April 2011)

We present and use an algorithm based on convex conic optimization to design two-dimensional photonic crystals with large absolute band gaps. Among several illustrations we show that it is possible to design photonic crystals which exhibit multiple absolute band gaps for the combined transverse electric and magnetic modes. The optimized crystals show complicated patterns which are far different from existing photonic crystal designs. We employ subspace approximation and mesh adaptivity to enhance computational efficiency. For some examples involving two band gaps, we demonstrate the tradeoff frontier between two different absolute band gaps.

DOI: 10.1103/PhysRevE.83.046703 PACS number(s): 02.60.Pn, 42.70.Qs

I. INTRODUCTION

Photonic crystals are periodic structures created from the arrangement of low and high index materials. They are designed to affect the motion of light by prohibiting the propagation of electromagnetic waves in all directions within certain frequency ranges known as *absolute band gaps* (ABGs). A *complete band gap* (CBG) refers to the case when the the ABG is independent of the polarization of the wave. Photonic band gap structures have proven very important as an enabling tool for the design and fabrication of many novel devices including frequency filters, waveguides, switches, and optical buffers [1–4]. Therefore the ability to design materials which have prescribed band gap diagrams is very important from a practical perspective.

It is well known that a low-index-hole (e.g., air-hole) two-dimensional (2D) photonic crystal has larger ABGs in transverse electric (TE) modes, while a high-index-hole 2D photonic crystal has larger ABGs in transverse magnetic (TM) modes. A detailed explanation for this behavior can be found in [5]. This observation has been extensively used to create a wide variety of photonic structures [6,7]. However, the structures created using parametric studies combined with physical reasoning are in general not optimal and larger band gaps can often be obtained when using formal topology optimization methods. Previous topology approaches include gradient-based approaches [8–10] and evolutionary methods [11,12]. Although these methods have been used to produce useful designs, the band gap optimization problem is a difficult nonconvex optimization problem, and first-order (and other gradient-based) methods suffer from low regularity and nondifferentiability due to the presence of eigenvalue multiplicities.

Recently, the work of [13] has used extensive numerical optimization to produce designs of photonic structures with very large ABGs for the first 15 bands. In particular, the authors therein propose a simple geometric scheme that provides structures with very large gaps between any two bands. They conjecture that the globally optimal structure for TM modes is the triangular distribution of circular rods and that the globally optimal structure for TE modes is a triangular distribution of hexagonal (instead of the commonly used circular) holes, i.e., the honeycomb structure. Interestingly, corroborative evidence for this line of conjecture can be found in the current paper's antecedent work [14], which used semidefinite programming and subspace methods as the enabling tools for more general (though still nonconvex) design optimization. However, it should be noted that the geometric scheme in [13] is not applicable to the combined TE and TM (CBG) gaps, and in fact, using extensive optimization, no systematic approach to CBG design was found in [13].

In this paper, we aim to optimally design photonic crystals which possess ABGs in several frequency bands (i.e., multiple ABGs) and in combined TE and TM modes (i.e., multiple CBGs). A photonic crystal structure exhibiting multiple CBGs is of considerable interest because it enables novel photonic devices to operate with a wider range of forbidden frequencies and in both TE and TM modes. For instance, a material for which propagation is forbidden at integer multiples of a fundamental frequency could prove useful for the design of resonant cavities. Our optimization algorithm is an extension of the work in [14], which uses convex conic (semidefinite) optimization as a subroutine in a broader nonconvex optimization scheme that aims to compute optimal solutions. We consider both square lattice and hexagonal lattice arrangements. Our algorithm computes crystal design patterns which may be very different from existing photonic crystals, yet many of which are simple enough to be fabricated using current state-of-the-art technology. Moreover, the relative efficiency of our algorithm allows extra exploration of the design space and thus increases the likelihood that larger local (and possibly global) optimal solutions are computed. For some examples involving two band gaps, we estimate the tradeoff frontier to demonstrate the tradeoff in design between two different absolute band gaps.

Extensive analysis has generally revealed the dictum that "the TM band gaps are favored in lattices of isolated high-ϵ regions, and TE band gaps are favored in connected lattices" [5], and indeed this has been validated in [10,13,14] for single-gap photonic crystals. The computation of multiple ABG designs herein further validates this statement for a large number of examples except for the TE case where we obtain

nonconnected structures supporting multiple band gaps. This observation raises a dilemma for the polarization-independent CBGs as it seems that both the isolation of high-ϵ and the connectedness of the structure can be satisfied only in a triangular lattice arrangement [5]. The recent work of [15] has investigated both absolute and complete band gaps for two-dimensional semiconductor-dielectric photonic crystals as a function of the filling fraction. By considering photonic crystals made up of doped-GaAs cylinders ($\epsilon_r = 12.8$) embedded in a vacuum background ($\epsilon_a = 1$), the authors therein found that the semiconductor-dielectric structure supports multiple ABGs at the filling fraction of 47.5% for a square lattice and at the filling fraction of 52.5% for a hexagonal lattice. However, they could find only a single CBG for a specific filling fraction and the magnitude of the gap-midgap ratio of approximately 1% is very small. In this paper, we demonstrate that for the same materials, our optimization algorithm yields not one, but two complete band gaps with significantly larger gap-midgap ratios, on the order of 6% or more.

The paper is organized as follows. In Sec. II, we present the photonic crystal design optimization problem and present our algorithm for computing large band gap designs. In Sec. III, we present a mesh adaptivity methodology as well as a summary of our computational scheme. In Sec. IV, we present selected results, including adaptive computational mesh, crystal design with multiple band gaps in TE, TM, and combined TEM polarizations, and in square as well as hexagonal lattices.

II. PHOTONIC CRYSTAL DESIGN VIA CONSTRAINED OPTIMIZATION

We first review basic terminology, notation, and modeling framework from [14]. A two-dimensional photonic crystal is characterized by having a dielectric function $\epsilon(\boldsymbol{r})$ which is periodic in the xy plane and constant in the z direction, i.e., $\epsilon(\boldsymbol{r}) = \epsilon(\boldsymbol{r} + \boldsymbol{R}_d)$, where $\boldsymbol{R}_d$, $(d = 1,2)$, are primitive lattice vectors depending on the periodicity length a of the lattice. The electromagnetic modes of a two-dimensional crystal can be classified into two different polarizations: transverse magnetic (TM) (electric field in the z direction) and transverse electric (TE) (magnetic field in the z direction). These two types of modes can be described by two scalar wave equations [14]. Assuming periodicity of the solution in the xy plane, the Floquet-Bloch theory shows that the scalar fields satisfy a Hermitian eigenvalue equation in a unit cell of the form

$$\mathcal{A}u = \lambda \mathcal{M}u \quad \text{in } \Omega. \tag{1}$$

For the TE mode, we have $u \equiv H_z(\boldsymbol{r})$, $\lambda \equiv \omega^2/c^2$, and

$$\mathcal{A}(\epsilon,\boldsymbol{k}) \equiv -(\nabla + i\boldsymbol{k}) \cdot [\epsilon^{-1}(\boldsymbol{r})(\nabla + i\boldsymbol{k})], \quad \mathcal{M} \equiv I,$$

where c is the speed of light, I denotes the identity operator, and the wave vector $\boldsymbol{k}$ lies in the irreducible Brillouin zone $\mathcal{B}$. For the TM mode, we have $u \equiv E_z(\boldsymbol{r})$, $\lambda \equiv \omega^2/c^2$, and

$$\mathcal{A}(\boldsymbol{k}) \equiv -(\nabla + i\boldsymbol{k}) \cdot (\nabla + i\boldsymbol{k}), \quad \mathcal{M}(\epsilon) \equiv \epsilon(\boldsymbol{r})I.$$

The unit cell Ω and the irreducible Brillouin zone $\mathcal{B}$ depend on the lattice type [5]. We denote by (u^m,λ^m) the mth eigenfunction-eigenvalue pair of Eq. (1) and assume that these eigenpairs are numbered in ascending order: $0 < \lambda^1 \leqslant \lambda^2 \leqslant \ldots \leqslant \lambda^\infty$.

Let $\mathcal{J} = \{m_j \mid j = 1,2,\ldots,J\}$ denote a set of J bands for which we seek to achieve absolute gaps. For instance, $\mathcal{J} = \{1,3,5\}$ indicates the set of the first, third, and fifth band gaps corresponding to $m_1 = 1, m_2 = 3$, and $m_3 = 5$. We define the *eigenvalue gap-midgap* ratio between bands m_j and $m_j + 1$ as

$$R^j(\epsilon(\boldsymbol{r})) = 2\,\frac{\inf\limits_{k\in\mathcal{B}} \lambda^{m_j+1}(\epsilon(\boldsymbol{r}),\boldsymbol{k}) - \sup\limits_{k\in\mathcal{B}} \lambda^{m_j}(\epsilon(\boldsymbol{r}),\boldsymbol{k})}{\inf\limits_{k\in\mathcal{B}} \lambda^{m_j+1}(\epsilon(\boldsymbol{r}),\boldsymbol{k}) + \sup\limits_{k\in\mathcal{B}} \lambda^{m_j}(\epsilon(\boldsymbol{r}),\boldsymbol{k})}.$$

We therefore consider the following optimization problem:

$$\sup_{\epsilon(\boldsymbol{r})\in\mathcal{Q}} \inf_{1\leqslant j\leqslant J} \alpha_j\, R^j(\epsilon(\boldsymbol{r}))\,. \tag{2}$$

Here $\mathcal{Q} \equiv \{\epsilon(\boldsymbol{r}) : \epsilon(\boldsymbol{r}) \in [\epsilon_L,\epsilon_H],\ \forall \boldsymbol{r} \in \Omega\}$ is the admissible domain, where ϵ_L and ϵ_H are dielectric constants of a low-index material and a high-index material, respectively. The α_j are prescribed weights for each band gap (though in our computation we typically set $\alpha_j = 1,\ j = 1,\ldots,J$). Thus the objective in Eq. (2) is to find an optimal material distribution that maximizes the (weighted) smallest gap among J chosen bands.

In practice, we discretize the optimization problem (2) as follows. First, we consider only n_k wave vectors in the set

$$\mathcal{P}_h = \{\boldsymbol{k}_k \in \partial\mathcal{B},\ 1 \leqslant k \leqslant n_k\}, \tag{3}$$

where $\partial\mathcal{B}$ represents the boundary of the irreducible Brillouin zone. Second, the unit cell Ω is discretized into $N \times N$ elements on which the dielectric function takes a piecewise constant value between ϵ_L and ϵ_H on each element; moreover, if the symmetry of the prescribed lattice is taken into consideration, the dielectric function only needs to be defined in 1/8 of the unit cell in a square lattice, or in 1/12 of the unit cell in a hexagonal lattice, namely,

$$\mathcal{Q}_h \equiv \{\boldsymbol{\epsilon} : \boldsymbol{\epsilon} \in [\epsilon_L,\epsilon_H]^{n_\epsilon}\}, \tag{4}$$

where $n_\epsilon < N^2 \equiv \mathcal{N}$. Third, we use a Galerkin finite element method with piecewise linear polynomials to approximate the system (1) as

$$A_h(\boldsymbol{\epsilon},\boldsymbol{k})u_h^{m_j} = \lambda_h^{m_j} M_h(\boldsymbol{\epsilon})u_h^{m_j}, \quad \boldsymbol{\epsilon} \in \mathcal{Q}_h, \boldsymbol{k} \in \mathcal{P}_h, \tag{5}$$

where $A_h(\boldsymbol{\epsilon},\boldsymbol{k}) \in \mathbb{C}^{\mathcal{N}\times\mathcal{N}}$ is a Hermitian matrix and $M_h(\boldsymbol{\epsilon}) \in \mathbb{R}^{\mathcal{N}\times\mathcal{N}}$ is a symmetric positive definite matrix. Since $\epsilon(\boldsymbol{r})$ is piecewise constant on Ω, the ϵ-dependent matrices can be expressed as

$$A_h^{\mathrm{TE}}(\boldsymbol{\epsilon},\boldsymbol{k}) = \sum_{i=1}^{n_\epsilon} \epsilon_i^{-1} A_{h,i}^{\mathrm{TE}}(\boldsymbol{k}), \quad M_h^{\mathrm{TM}}(\boldsymbol{\epsilon}) = \sum_{i=1}^{n_\epsilon} \epsilon_i M_{h,i}^{\mathrm{TM}} \tag{6}$$

while $A_h^{\mathrm{TM}}(\boldsymbol{k})$ and M_h^{TE} are independent of ϵ. Here and below, superscripts $^{\mathrm{TM}}$ and $^{\mathrm{TE}}$ are used to indicate TM polarization and TE polarization, respectively.

For the TE case, we define the discrete *eigenvalue gap-midgap* ratio between eigenvalues m_j and m_j+1 as

$$R_h^{\mathrm{TE},j}(\boldsymbol{\epsilon}) = 2\,\frac{\min\limits_{k\in\mathcal{P}_h}\lambda_h^{\mathrm{TE},m_j+1}(\boldsymbol{\epsilon},\boldsymbol{k}) - \max\limits_{k\in\mathcal{P}_h}\lambda_h^{\mathrm{TE},m_j}(\boldsymbol{\epsilon},\boldsymbol{k})}{\min\limits_{k\in\mathcal{P}_h}\lambda_h^{\mathrm{TE},m_j+1}(\boldsymbol{\epsilon},\boldsymbol{k}) + \max\limits_{k\in\mathcal{P}_h}\lambda_h^{\mathrm{TE},m_j}(\boldsymbol{\epsilon},\boldsymbol{k})}.$$

For the TM case the discrete *eigenvalue gap-midgap* ratio $R_h^{\mathrm{TM},j}(\boldsymbol{\epsilon})$ is defined in a similar manner. For the *complete* band gaps we define the discrete *eigenvalue gap* ratio between bands m_j and m_j+1 as

$$R_h^{j}(\boldsymbol{\epsilon}) = \min\left[R_h^{\mathrm{TE},j}(\boldsymbol{\epsilon}),\quad R_h^{\mathrm{TM},j}(\boldsymbol{\epsilon})\right].$$

To design the photonic crystal structure that supports multiple combined band gaps we propose to solve the following optimization problem:

$$\begin{gathered}\max_{\epsilon\in\mathcal{Q}_h}\min_{1\leqslant j\leqslant J}\alpha_j\,R_h^j(\boldsymbol{\epsilon}),\quad \text{s.t.}\\ A_h^{\mathrm{TE}}(\boldsymbol{\epsilon},\boldsymbol{k})u_h^{\mathrm{TE},m_j} = \lambda_h^{\mathrm{TE},m_j}M_h^{\mathrm{TE}}(\boldsymbol{\epsilon})u_h^{\mathrm{TE},m_j},\\ A_h^{\mathrm{TM}}(\boldsymbol{\epsilon},\boldsymbol{k})u_h^{\mathrm{TM},m_j} = \lambda_h^{\mathrm{TM},m_j}M_h^{\mathrm{TM}}(\boldsymbol{\epsilon})u_h^{\mathrm{TM},n_j},\\ \text{for}\ \ j=1,\ldots,J,\boldsymbol{k}\in\mathcal{P}_h.\end{gathered}\tag{7}$$

To model only TE or TM polarization, one can simply omit the nonrelevant equations in the above formulation. Note further that the formulation (7) can be generalized to treat more general cases in which the number and location of TE band gaps are allowed to differ from those of TM band gaps.

In the previous work [14], we showed how to use semidefinite inclusions combined with subspace methods to locally approximate the single ABG problem [only one band gap and either TE or TM polarization, which is simpler than Eq. (7)] as a convex semidefinite program; see Sec. 3.3.1 of [14]. We now indicate how extensions of these ideas can be used to develop a tractable (i.e., conic and convex) local approximation of Eq. (7). It will be convenient to consider the change of variables defined by $\gamma_j = 1/\epsilon_j$, $j=1,\ldots,n_\epsilon$. Let $\hat{\boldsymbol{\epsilon}}$ be a given parameter vector satisfying $\hat{\boldsymbol{\epsilon}}\in\mathcal{Q}_h$ and define $\hat{\gamma}_j = 1/\hat{\epsilon}_j$, $j=1,\ldots,n_\epsilon$. Then the following optimization problem is an extension of approximations (16) and (17) developed in [14]:

$$\begin{aligned}\max_{y}\quad & F\\ \text{s.t.}\quad & \Phi_{m_j}^{\mathrm{TE}*}(\hat{\boldsymbol{\gamma}},\boldsymbol{k})\left[A_h^{\mathrm{TE}}(\boldsymbol{\gamma},\boldsymbol{k}) - b_j M_h^{\mathrm{TE}}\right]\Phi_{m_j}^{\mathrm{TE}}(\hat{\boldsymbol{\gamma}},\boldsymbol{k}) \preceq 0,\\ & \Psi_{m_j}^{\mathrm{TE}*}(\hat{\boldsymbol{\gamma}},\boldsymbol{k})\left[A_h^{\mathrm{TE}}(\boldsymbol{\gamma},\boldsymbol{k}) - a_j M_h^{\mathrm{TE}}\right]\Psi_{m_j}^{\mathrm{TE}}(\hat{\boldsymbol{\gamma}},\boldsymbol{k}) \succeq 0,\\ & \Phi_{m_j}^{\mathrm{TM}*}(\hat{\boldsymbol{\epsilon}},\boldsymbol{k})\left[d_j A_h^{\mathrm{TM}}(\boldsymbol{k}) - M_h^{\mathrm{TM}}(\boldsymbol{\epsilon})\right]\Phi_{m_j}^{\mathrm{TM}}(\hat{\boldsymbol{\epsilon}},\boldsymbol{k}) \preceq 0,\\ & \Psi_{m_j}^{\mathrm{TM}*}(\hat{\boldsymbol{\epsilon}},\boldsymbol{k})\left[c_j A_h^{\mathrm{TM}}(\boldsymbol{k}) - M_h^{\mathrm{TM}}(\boldsymbol{\epsilon})\right]\Psi_{m_j}^{\mathrm{TM}}(\hat{\boldsymbol{\epsilon}},\boldsymbol{k}) \succeq 0,\\ & F \leqslant \alpha_j\left(2\tfrac{a_j-b_j}{a_j+b_j}\right),\\ & F \leqslant \alpha_j\left(2\tfrac{d_j-c_j}{d_j+c_j}\right),\\ & \epsilon_i\gamma_i = 1,\\ & a_j\geqslant 0, b_j\geqslant 0, c_j\geqslant 0, d_j\geqslant 0,\\ & \boldsymbol{\epsilon}\in\mathcal{Q}_h,\boldsymbol{\gamma}\in\mathcal{S}_h,\boldsymbol{k}\in\mathcal{P}_h,\ \text{and}\ j\in\{1,\ldots,J\},\\ & i=1,\ldots,n_\epsilon,\end{aligned}\tag{8}$$

where $\boldsymbol{y} = [\boldsymbol{\epsilon},\boldsymbol{\gamma},\boldsymbol{a},\boldsymbol{b},\boldsymbol{c},\boldsymbol{d},F]$ and $\mathcal{S}_h \equiv \{\boldsymbol{\gamma} : \boldsymbol{\gamma}\in[1/\epsilon_H,1/\epsilon_L]^{n_\epsilon}\}$.

As developed in [14], the matrices $\Phi_{m_j}^{\mathrm{TE}}(\hat{\boldsymbol{\gamma}},\boldsymbol{k})$ and $\Psi_{m_j}^{\mathrm{TE}}(\hat{\boldsymbol{\gamma}},\boldsymbol{k})$, [respectively, $\Phi_{m_j}^{\mathrm{TM}}(\hat{\boldsymbol{\epsilon}},\boldsymbol{k})$ and $\Psi_{m_j}^{\mathrm{TM}}(\hat{\boldsymbol{\epsilon}},\boldsymbol{k})$] ideally are comprised columnwise of the lower m_j eigenvectors and the upper $\mathcal{N}-m_j$ eigenvectors of Eq. (5) for the TE case (respectively, the TM case). As developed in [14], we instead work with a small "important" subset of these eigenvectors to keep the computation efficient; see [14] for details. The semidefinite inclusions [the first four sets of constraints in Eq. (8)] are linear in the design variables $\boldsymbol{y}$. The bilinear constraints [the fifth through seventh set of constraints in Eq. (8)] can be linearized around the previous solution to obtain a linear semidefinite program. For instance, the constraint $\epsilon_i\gamma_i = 1$ is linearized as $\hat{\epsilon}_i\hat{\gamma}_i + \hat{\epsilon}_i(\gamma_i-\hat{\gamma}_i) + \hat{\gamma}_i(\epsilon_i-\hat{\epsilon}_i) = 1$. The resulting linearized semidefinite program can be efficiently solved using modern interior point methods such as the SDPT3 software [16].

III. MESH ADAPTIVITY AND COMPUTATIONAL PROCEDURE

We develop an adaptive mesh refinement algorithm in order to improve the efficiency and accuracy of discretization. Rather than using a uniform computational mesh, we employ a discretization adapted to the particular material distribution that is being computed. Given any initial coarse representation of the optimal configuration, we choose and subdivide elements that meet the refinement criteria. In particular, elements are refined when they are on the material interface, i.e., when there is a jump in the value of the design variables between the element under consideration and at least one of its neighbors. When an element is refined, hanging nodes are generated if the neighboring elements are of different sizes after refinement. In order to simplify the computational procedure, we impose a 2:1 rule to restrict the refinement level difference between neighboring elements: if the refinement level difference exceeds 2, the larger element is further refined such that at most one hanging node exists on any element edge. In order to ensure a continuous finite element interpolation, the degree of freedom corresponding to the hanging node is constrained to the interpolated value from the two corner nodes and can therefore be locally eliminated from the global system.

Our computational procedure incorporating mesh adaptivity in conjunction with the local optimization problem (8) is as follows:

(1) Start with a coarse mesh 8×8 and a random initial distribution $\hat{\boldsymbol{\epsilon}}$, and an error tolerance ϵ_{tol};

(2) if necessary, use interpolation to adapt the current distribution $\hat{\boldsymbol{\epsilon}}$ to correspond to the current refined mesh;

(3) for each wave vector $\boldsymbol{k}\in P_h$, compute the subspaces $\Phi_{m_j}^{\mathrm{TE}}(\hat{\boldsymbol{\epsilon}},\boldsymbol{k})$, $\Psi_{m_j}^{\mathrm{TE}}(\hat{\boldsymbol{\epsilon}},\boldsymbol{k})$, $\Phi_{m_j}^{\mathrm{TM}}(\hat{\boldsymbol{\gamma}},\boldsymbol{k})$, and $\Psi_{m_j}^{\mathrm{TM}}(\hat{\boldsymbol{\gamma}},\boldsymbol{k})$, and form the linearized version of the semidefinite program (8);

(4) solve the linearized version of Eq. (8) for an optimal solution $\boldsymbol{\epsilon}^*$;

(5) *if* $\|\boldsymbol{\epsilon}^*-\hat{\boldsymbol{\epsilon}}\|\leqslant\epsilon_{\mathrm{tol}}$, and *current refinement level* $<$ *maximum refinement level*, *then* refine elements adaptively, extrapolate $\boldsymbol{\epsilon}^*\to\hat{\boldsymbol{\epsilon}}$ of the new mesh, and go to 1;

(6) *else if* $\|\boldsymbol{\epsilon}^*-\hat{\boldsymbol{\epsilon}}\|>\epsilon_{\mathrm{tol}}$, and *current refinement level* $\leqslant$ *maximum refinement level*, *then* update $\hat{\boldsymbol{\epsilon}}\leftarrow\boldsymbol{\epsilon}^*$, and go to 2;

(7) *else if* $\|\boldsymbol{\epsilon}^*-\hat{\boldsymbol{\epsilon}}\|\leqslant\epsilon_{\mathrm{tol}}$, and *current refinement level* $\geqslant$ *maximum refinement level*, *then* stop and return optimal $\boldsymbol{\epsilon}^*$.

IV. RESULTS AND DISCUSSION

We present computational results for the design of photonic crystals made up of doped GaAs ($\epsilon_r = 12.8$) and vacuum air ($\epsilon_a = 1$) [10,15]. We computed a wide variety of optimized pairs and triplets of multiple band gaps in TE, TM, and complete TEM modes, for both square and hexagonal lattices. In the results presented herein, the eigenvalues are plotted in the dimensionless unit $(\omega a/2\pi c)^2$, where a is the lattice constant for both square and hexagonal lattices. For comparison between our results and other previous results, we also describe our results in terms of the *frequency gap-midgap* ratio between bands m_j and $m_j + 1$, defined as

$$Q_h^j \equiv \frac{\Delta\omega_h^{m_j}}{\overline{\omega}_h^{m_j}} = 2\,\frac{\min\limits_{k\in\mathcal{P}_h}\omega_h^{m_j+1}(\boldsymbol{\epsilon},\boldsymbol{k}) - \max\limits_{k\in\mathcal{P}_h}\omega_h^{m_j}(\boldsymbol{\epsilon},\boldsymbol{k})}{\min\limits_{k\in\mathcal{P}_h}\omega_h^{m_j+1}(\boldsymbol{\epsilon},\boldsymbol{k}) + \max\limits_{k\in\mathcal{P}_h}\omega_h^{m_j}(\boldsymbol{\epsilon},\boldsymbol{k})}.$$

The frequency gap-midgap ratio is used as the objective function in some published research (see, e.g., [10,15]), while the eigenvalue gap-midgap ratio is used in other published research (e.g., [9,13,14]). Despite the obvious difference between the eigenvalue and frequency (the former being the square of the latter divided by the speed of light), the optimal crystal structures have been observed to be astonishingly consistent when either is used in the gap objective function in single band gap optimization problems [10,13,14]. While it is intuitive that the frequency relative gap-midgap ratio should be monotone in the eigenvalue gap-midgap ratio, one can create pathological counterexamples. Herein we choose to optimize the eigenvalue gap-midgap ratio because the first four sets of constraints of our optimization model (8) are linear in the eigenvalues and so require no extra linearization themselves, and the fifth and sixth constraints are only modestly nonlinear in the eigenvalues. Of course, should one wish to optimize the frequency gap-midgap ratio, the resulting nonlinear constraints [the fifth and sixth set of constraints in Eq. (8)] could be linearized as discussed earlier when constructing the linear semidefinite program.

We initialize our procedure with a very coarse grid 8×8 and adaptively refine it up to 128×128 in resolution. We initialize with a random distribution $\hat{\boldsymbol{\epsilon}}$ on this coarse grid, and then obtain an optimal solution on the coarse grid 8×8; this optimal solution is used as the basis to refine the grid and is then adapted to the refined grid by interpolation as discussed in Sec. III. (A detailed discussion on the choice of some other simulation parameters can be found in our previous work [14]). We found that the grid refinement procedure significantly reduces both the number of degrees of freedom in the finite element procedure and the number of decision variables in the optimization procedure, thereby leading to a significant reduction in computation time, with a speedup in overall computation in the range 40% –500%, but typically around 250%. All computations were performed on a Linux PC with Dual Core AMD Opteron 270, 2.0 GHz, and each run of our procedure was obtained in 1–10 min. The relatively low computation times enabled us to study the inherent tradeoffs between optimizing two different band gaps (namely, the tradeoff frontier), which provides very useful information for choosing the most appropriate design. Below we present representative results to illustrate various aspects of solutions to the multiple and combined band gap optimization problem.

A. TM band gaps

We illustrate a typical sequence of optimal solutions using our mesh adaptivity procedure on the problem of optimizing the second and fifth band gaps [with identical weights, i.e., $(\alpha_1,\alpha_2) = (1,1)$] in the hexagonal lattice. Our results are shown in Fig. 1. It is important to note that grid resolution affects the obtained results. In particular, relatively coarse resolutions ($h_{\min} = a/8, a/16$) produce optimal solutions with some mixed features (i.e., $\epsilon_L < \epsilon_i < \epsilon_H$ for some cell elements i), while finer resolutions ($h_{\min} = a/32, a/64, a/128$) yield optimal structures which involve only pure concentrations ($\epsilon_i = \epsilon_L$ or ϵ_H for all cell elements i). Moreover, the shape of the circular inclusions is much more visible on the finer

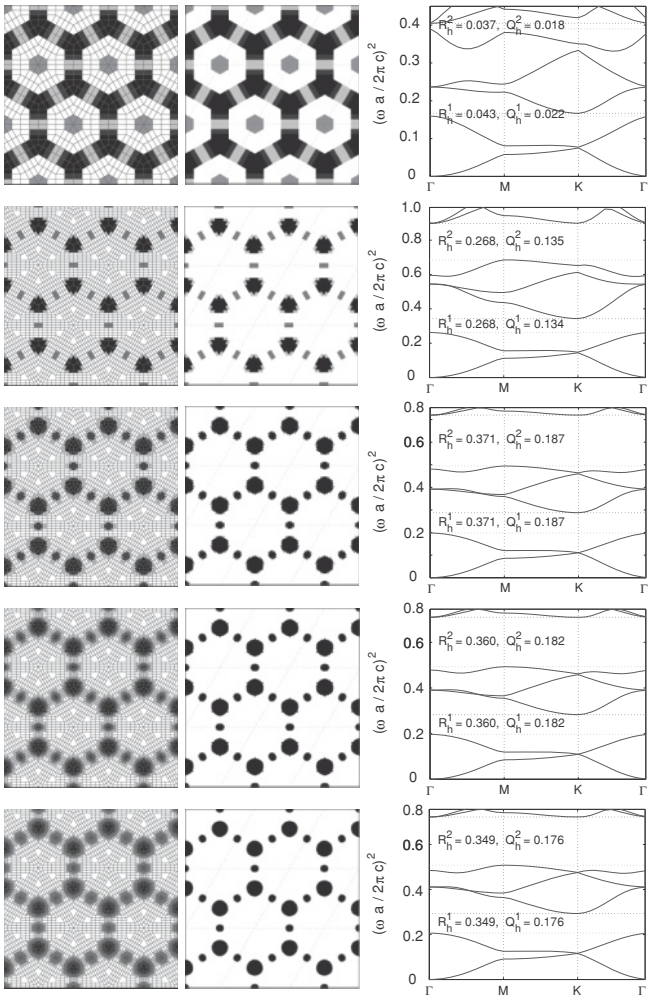

FIG. 1. Mesh adaptivity results show the computational grids overlaid on the crystal structures (left), optimal crystal structures (middle), and frequency bands (right) for the second and fifth TM band gaps in the hexagonal lattice. Grid resolution varies from $h_{\min} = a/8$ (top panel), $h_{\min} = a/16$ (second panel), $h_{\min} = a/32$ (third panel), $h_{\min} = a/64$ (four panel), to $h_{\min} = a/128$ (bottom panel). The letters Γ, M, and K in this figure and some figures below represent the vertices of the irreducible Brillouin zone of the hexagonal lattice.

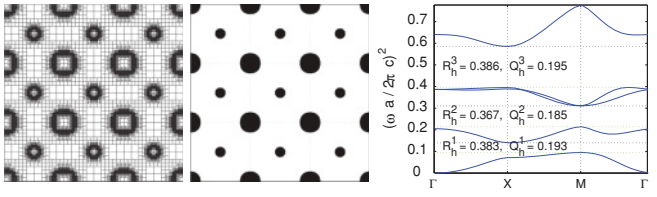

FIG. 2. (Color online) Optimization results show the final computational grid (left), optimal crystal structure (middle), and frequency bands (right) for the first, second, and fourth TM band gaps in the square lattice. The letters Γ, X, and M in this figure and some figures below represent the vertices of the irreducible Brillouin zone of the square lattice.

grids. Our optimized structure differs from existing single-gap photonic crystals [10,13,14] in the sense that it has both small inclusions (of radius $r_s/a = 0.06$) and large inclusions (of radius $r_l/a = 0.12$), while single-gap photonic crystals typically consist of inclusions of the same radius. It is interesting to observe that the unit cell of the optimized structure consists of two large circular disks and three small disks as we optimize the second and fifth band gaps.

A typical triplet of optimized band gaps is shown in Fig. 2, which presents the optimized structures for optimizing the first, second, and fourth band gaps (with identical weights $\alpha_1 = \alpha_2 = \alpha_3 = 1$) in the square lattice. In this case, the optimized structure also consists of circular disks of different sizes ($r_l/a = 0.17, r_s/a = 0.08$). Similar to the previous results, the relative eigenvalue gaps are the same for all three bands since we chose the same weights for all bands. One notable feature of this photonic structure is that the midgap frequency of the third band is approximately twice that of the first band.

In optimizing a weighted pair of band gaps, there is an intuitive tradeoff between the size of one band gap versus the other band gap that can be computed by varying the weights associated with each band to yield a tradeoff frontier between the two band gaps. Such a tradeoff frontier is illustrated in Fig. 3 for the problem of optimizing the weighted first and third band gaps in the hexagonal lattice. The points in the figure were produced by varying the weights (α_1,α_2) associated with two band gaps (first and third bands, respectively) for a variety of values of $(\alpha_1,\alpha_2) \in [0,1]^2$. More specifically, we start by computing a solution for $(\alpha_1,\alpha_2) = (0.5,0.5)$ on a uniform mesh 64×64. We then modify the weights $(\alpha_1,\alpha_2) \in [0,1]^2$ slightly and use the previously obtained solution as the initiating distribution for computing the solution for the problem with modified weights. This step is repeated in order to track various local optimal branches. Figure 3 illustrates the tradeoff frontiers A-B and C-D, where A, B, C, and D correspond to the optimized structures for $(\alpha_1,\alpha_2) = (0.99,0.01)$, $(0.01,0.99)$, $(0.99,0.01)$, and $(0.01,0.99)$, respectively. The figure shows two different frontiers A-B and C-D. The multiple branches of the frontiers represent multiple *significant* local optima corresponding to identical weights. Structure A favors the third band gap, whereas structure B favors the first band gap. Structure C exhibits a good compromise between the two band gaps since both are relatively large in this case. Structure C is particularly interesting in that it resembles D in overall design, but has larger disks with an air hole. Frontier A-B consists of structures having disks of two different radii but otherwise similar topology, while frontier C-D consists of structures having disks of different radii and different topology.

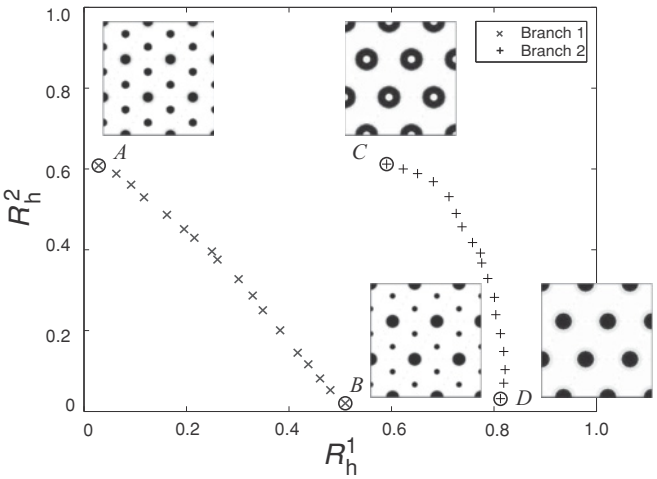

FIG. 3. The tradeoff frontier for the first (horizontal axis) and third (vertical axis) TM band gaps in the hexagonal lattice. The frontiers are traced by varying the weights corresponding to each band gap. Multiple frontiers can be attributed to multiple local optima.

B. TE band gaps

We now turn to TE band gaps. Figures 4 and 5 show typical results for optimizing pairs (first and second band gaps) and triplets (second, fourth, and sixth band gaps) in the square lattice, respectively, where all bands have equal weights. We observe that the optimized structure in Fig. 4 is connected and relatively simple, whereas the optimized structure in Fig. 5 is nonconnected and far more complicated. Although TE polarization typically favors connected lattices, these results show that it is possible to obtain nonconnected TE structures with multiple band gaps.

Figure 6 shows solutions for optimizing the first and fourth TE band gaps for both the square and hexagonal lattices (with equal weights for the two bands). We observe that the optimized structure in the square lattice is not connected, while the optimized structure in the hexagonal lattice is connected. Moreover, we see for both band structures that the midgap frequency of the fourth band is roughly twice that of the first band. Therefore similar to the structure shown in Fig. 2, these designs can prohibit electromagnetic waves at both frequencies ω and 2ω.

We also studied the tradeoff frontier for the first and third TE band gap in the hexagonal lattice; see Fig. 7. This

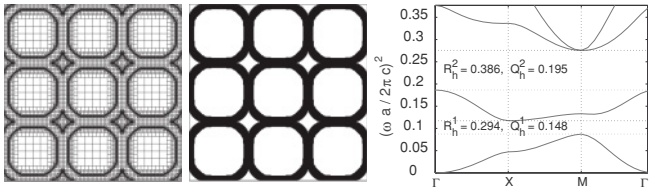

FIG. 4. Optimization results show the final computational grid (left), optimal crystal structure (middle), and frequency bands (right) for the first and second TE band gaps in the square lattice.

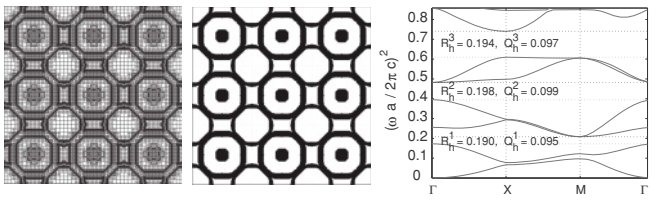

FIG. 5. Optimization results show the final computational grid (left), optimal crystal structure (middle), and frequency bands (right) for the second, fourth, and sixth TE band gaps in the square lattice.

frontier has proven to be more complicated than its TM mode counterpart shown previously in Fig. 3. In fact, no distinctive frontier can be observed, which is undoubtedly due to numerous local optima in this case. We employed a similar computational strategy to that used to produce Fig. 3 as described in the previous subsection. In Fig. 7 we display four (locally) optimized structures along the envelope *A*-*B*-*C*-*D* of the apparent frontier, where *A*, *B*, *C*, and *D* correspond to solutions for $(\alpha_1,\alpha_2) = (0.99,0.01)$, $(0.5,0.5)$, $(0.5,0.5)$, and $(0.01,0.99)$, respectively. Structure *A* favors the third band, whereas structure *D* favors the first band. Structures *B* and *C* offer a compromise between the two bands. Note further that the two structures *B* and *C* are very different despite the fact that they have similar objective values. (We also observed many local optimal solutions in our previous work on the optimal design of photonic crystals with single band gap [14].)

C. Complete band gaps

We are able to compute complete band gaps for both the hexagonal and square lattices; the band gaps in the hexagonal lattice lie in the first and third bands for the TE polarization, yet in the third and sixth bands for the TM polarization. Figure 8 illustrates the geometry and band structures for the

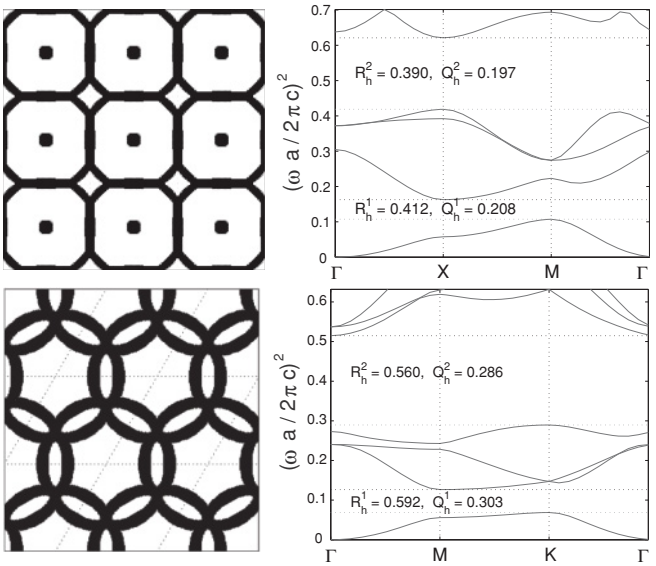

FIG. 6. Optimization results show optimal crystal structure (left), and frequency bands (right) for the first and fourth TE band gaps in the square lattice (top) and the hexagonal lattice (bottom).

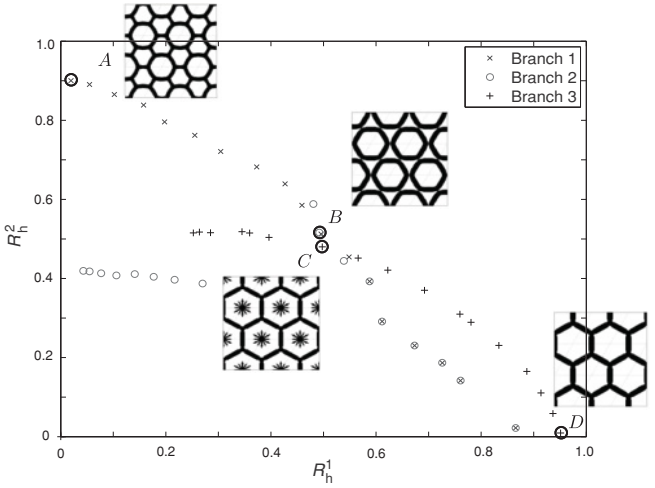

FIG. 7. The tradeoff frontier for the first (horizontal axis) and third (vertical axis) TE band gaps in the hexagonal lattice. The frontiers are traced by varying the weights corresponding to each band gap. Multiple frontiers can be attributed to multiple local optima.

hexagonal lattice. The corresponding *frequency gap-midgap ratios* of 5.76% and 6.94% are quite sizable—and are the first multiple and complete band gaps ever reported for photonic crystals in the hexagonal lattice. This photonic crystal structure has both connected and nonconnected features. Moreover, it has a more complicated geometry than the previous structures shown herein.

For the square lattice, complete band gaps lie in the third band for the TE polarization, yet in the sixth and ninth bands for the TM polarization. Figure 9 illustrates our results. The corresponding *frequency gap-midgap ratios* of 7.59% and 13.5% are also large. We emphasize again that no other multiple and complete gaps have previously been found for photonic crystals in the square lattice. In general, the complete band gaps are smaller than either of the corresponding TE and TM band gaps because it is rather difficult to simultaneously achieve both the TE and TM band gaps. Of course, one can also widen the gap size for one band at the expense of narrowing the gap size of the other band by choosing appropriate weights

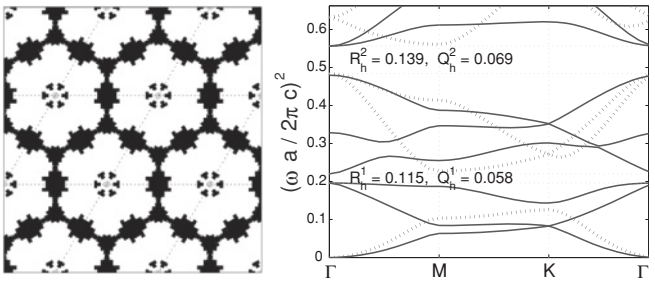

FIG. 8. Optimization results for the multiple complete band gaps in the hexagonal lattice. The optimal crystal structure is shown in the left-hand picture; while the frequency bands are shown in the right-hand picture, with solid lines representing TM bands, and broken lines representing TE bands. The first complete band gap is formed by the overlapping of the first TE and third TM band gaps, while the second complete band gap is formed by the third TE and sixth TM band gaps.

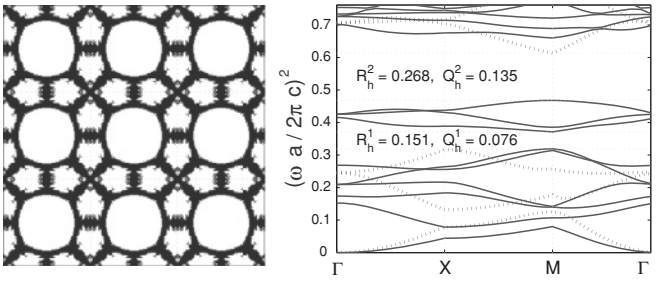

FIG. 9. Optimization results for the multiple complete band gaps in the square lattice. The optimal crystal structure is shown in the left-hand picture; while the frequency bands are shown in the right-hand picture, with solid lines representing TM bands, and broken lines representing TE bands. The first complete band gap is formed by the overlapping of the third TE and sixth TM band gaps, while the second complete band gap is formed by the third TE and ninth TM band gaps.

in the optimization problem (8). Finally, it is interesting to note in this case that although the photonic crystal structure has a complicated geometry, it is nevertheless connected.

V. CONCLUSIONS

In conclusion, we have demonstrated the usefulness of a computational scheme based on conic (semidefinite) convex optimization to design photonic crystals with multiple and complete band gaps in both square and hexagonal lattices. Our photonic crystal patterns are different from existing photonic crystal designs [10,13,14] with a single band gap. In particular, we observe from our results that unlike optimal photonic crystals discovered in [13], photonic crystals with multiple band gaps do not follow some simple geometric properties. Therefore numerical optimization is crucial to the design of photonic crystals that support several band gaps. These photonic crystals may prove useful for the suppression of resonance at harmonic frequencies, as they prohibit the propagation of electromagnetic waves at several different frequencies. In addition, we have computed photonic structures with large complete band gaps. Our results hopefully open up a new arena for the design of photonic crystals.

We note that many of the optimized crystal designs shown herein involve intricate patterns of materials at the nano-level, and may be too expensive or even impossible to fabricate. Simply incorporating "fabrication constraints" such as connectedness of materials or bounds on the curvature of boundaries easily yields combinatorially intractable optimization models. Instead, we propose to modify the basic optimization problem so that a resulting solution is "robust" for fabrication, somewhat in the spirit of robust convex optimization [17]. This is the subject of ongoing research.

ACKNOWLEDGMENTS

We are grateful to Steven Johnson of the MIT Mathematics Department for numerous discussions on this research. This research has been supported through AFOSR Grant No. FA9550-08-1-0350 and the Singapore-MIT Alliance.

[1] S. Fan, P. Villeneuve, J. Joannopoulos, and H. Haus, Opt. Express **3**, 4 (1998).
[2] S. Fan, J. D. Joannopoulos, J. N. Winn, A. Devenyi, J. C. Chen, and R. D. Meade, J. Opt. Soc. Am. B **12**, 1267 (1995).
[3] M. Soljacic, M. Ibanescu, S. G. Johnson, Y. Fink, and J. D. Joannopoulos, Phys. Rev. E **66**, 055601 (2002).
[4] M. F. Yanik and S. Fan, Phys. Rev. A **71**, 013803 (2005).
[5] J. D. Joannopoulos, S. G. Johnson, J. N. Winn, and R. D. Meade, *Photonic Crystals: Molding the Flow of Light* (Princeton University Press, Princeton, NJ, 2008).
[6] M. Doosje, B. J. Hoenders, and J. Knoester, J. Opt. Soc. Am. B **17**, 600 (2000).
[7] X. L. Yang, L. Z. Cai, Y. R. Wang, C. S. Feng, G. Y. Dong, X. X. Shen, X. F. Meng, and Y. Hu, Europhys. Lett. **81**, 14001 (2008).
[8] S. J. Cox and D. C. Dobson, J. Comput. Phys. **158**, 214 (2000).
[9] O. Sigmund and J. S. Jensen, Phil. Trans. R. Soc. Lond. A **361**, 1001 (2003).
[10] C. Y. Kao, S. Osher, and E. Yablonovitch, Appl. Phys. B: Lasers Opt. **81**, 235 (2005).
[11] L. Shen, Z. Ye, and S. He, Phys. Rev. B **68**, 035109 (2003).
[12] S. Preble, M. Lipson, and H. Lipson, Appl. Phys. Lett. **86**, 061111 (2005).
[13] O. Sigmund and K. Hougaard, Phys. Rev. Lett. **100**, 153904 (2008).
[14] H. Men, N. Nguyen, R. Freund, P. Parrilo, and J. Peraire, J. Comput. Phys. **229**, 3706 (2010).
[15] M. Martinez, J. Opt. Soc. Am. B **23**, 1460 (2006).
[16] R. H. Tütüncü, K. C. Toh, and M. J. Todd, Math. Program. **95**, 189 (2003).
[17] A. Ben-Tal and A. Nemirovski, Math. Oper. Res. **23**, 769 (1998).